



Epitaxial growth of few-layer MoS₂(0001) on FeS₂{100}†

T. Liu, I. Temprano, D. A. King, S. M. Driver* and S. J. Jenkins

Cite this: *Chem. Commun.*, 2015, 51, 537Received 22nd August 2014,
Accepted 13th November 2014

DOI: 10.1039/c4cc06628f

www.rsc.org/chemcomm

Physical vapour deposition of Mo on an FeS₂{100} surface was performed at 170 K. Near-epitaxial growth of MoS₂(0001) overlayers of the order of 1 nm thickness was observed when the Mo-covered substrate was subsequently heated to 600 K.

Graphene is currently the most widely studied two-dimensional material due in particular to its remarkable electronic properties. However, pristine graphene has the disadvantage that it lacks a bandgap, a property that is essential for many electronic applications.¹ Among alternative 2D materials, single-layer MoS₂ has arisen as a promising candidate as it has an intrinsic direct bandgap of 1.8 eV (*cf.* an indirect gap of 1.2 eV in bulk MoS₂) and thermal stability up to 1100 °C.² MoS₂ is also widely used in industry for its tribological properties (*e.g.* as a lubricant) and catalytic properties (*e.g.* in hydrodesulphurisation).³ Recent studies have indeed demonstrated the potential of 2D MoS₂ in device applications such as field effect transistors,⁴ optoelectronics,⁵ spintronics and 'valleytronics',⁶ and piezotronics.⁷

To exploit 2D materials for device applications, it is important to develop methods of preparing large-area, well ordered layers. Bottom-up synthesis methods based on chemical vapour deposition (CVD) or self-assembled monolayers have already shown promise in delivering high quality graphene.⁸ Few-layer MoS₂ is most commonly obtained by top-down methods such as lithium intercalation, micro mechanical exfoliation, or liquid-phase exfoliation.² Attempts to grow high-quality MoS₂ layers *via* CVD on different surfaces have yielded mixed results so far. For example, large area MoS₂ atomic layers have been produced on insulating surfaces (sapphire and SiO₂) and on graphene,⁹ whereas MoS₂ nanoclusters were found to form when Mo was deposited on Au{111} or HOPG under a pressure of H₂S.¹⁰

Here, we describe facile bottom-up epitaxial growth of a highly ordered MoS₂(0001) film, of the order of 1 nm thick, on a semiconducting substrate: this has not, to our knowledge, been reported before. It was achieved by physical vapour deposition (PVD) under ultra-high vacuum (UHV) on {100} surfaces of FeS₂ (iron pyrite). FeS₂ is of considerable interest in its own right for its electronic and optical properties, in view of its natural abundance. Moreover, the epitaxy points strongly to FeS₂/MoS₂ interface structure that is crystallographically well defined: this is likely to be beneficial for device applications in terms of its electronic properties and charge transport behaviour.¹¹

Our experiments were performed under UHV (base pressure $\sim 1 \times 10^{-10}$ mbar) in an apparatus described elsewhere.¹² As-grown {100} surfaces of naturally occurring FeS₂ crystals (Manchester Minerals) were used as substrates; these were prepared as described previously to obtain a highly-ordered stoichiometric termination.¹² The maximum temperature was kept below 630 K to avoid decomposition of the pyrite crystal. Mo was deposited by evaporation from a Mo rod (Goodfellow, 1.0 mm diameter, 99.99% purity), electron beam heated within an evaporator (Omicron EFM3) operated at 910 eV and 40 mA emission.

Stepwise deposition of Mo (with the substrate held at 170 K during deposition, followed by a flash anneal to 600 K after each deposition step) on pristine FeS₂{100} was monitored by Auger electron spectroscopy (AES). Mo/S and Fe/S Auger peak height ratios are displayed in Fig. 1 as a function of Mo deposition time. The cumulative deposition of Mo is reflected in a linear increase of the Mo/S ratio. The Fe/S ratio, by contrast, decreased quickly and linearly up to 9 min Mo deposition. Thereafter, the Fe/S ratio remained approximately constant at less than 10% of its initial value. At this point the Fe₅₀ Auger signal of the FeS₂{100} substrate is almost totally blocked by the deposited layer. This, in turn, implies that the outermost surface region has been transformed from iron sulphide to a layer of molybdenum sulphide. It is important to note that no S was introduced from external sources in this work. The only S available to react with the deposited metallic Mo layer must therefore have come from the pyrite crystal. Thermal diffusion of S from the bulk has been previously reported to cause recovery of the stoichiometry on S-depleted FeS₂{100} surfaces.¹²

Department of Chemistry, University of Cambridge, Lensfield Road, Cambridge, CB2 1EW, UK. E-mail: smd37@cam.ac.uk; Fax: +44 (0)1223 336362; Tel: +44 (0)1223 336503

† Electronic supplementary information (ESI) available: Digitally enhanced and energy-dependent LEED data, schematic of subsidiary overlayer structure, electron attenuation length calculation. See DOI: 10.1039/c4cc06628f



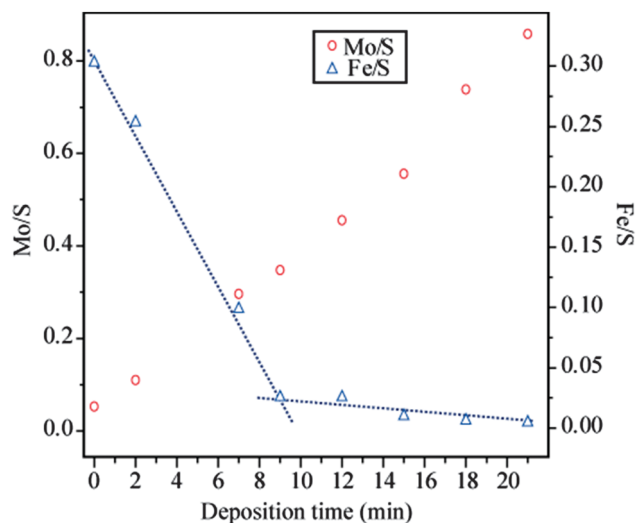


Fig. 1 Mo/S and Fe/S Auger peak height ratios (measured for the Mo peak at 190 eV kinetic energy, the Fe peak at 50 eV and the S peak at 155 eV) as a function of Mo deposition time on $\text{FeS}_2\{100\}$ surface (substrate was flash-annealed to 600 K between successive deposition steps).

The structural characteristics of the molybdenum sulphide overlayer were monitored by means of low energy electron diffraction (LEED). For the clean surface prior to Mo deposition, a diffraction pattern with a square array of sharp spots is observed, consistent with the (1×1) lattice of bulk-terminated $\text{FeS}_2\{100\}$. The spot sharpness was routinely monitored and provides a qualitative indication of the surface order of the substrate prior to and after exposure to Mo. Fig. 2a shows the diffraction pattern of the surface after 2 min Mo deposition,

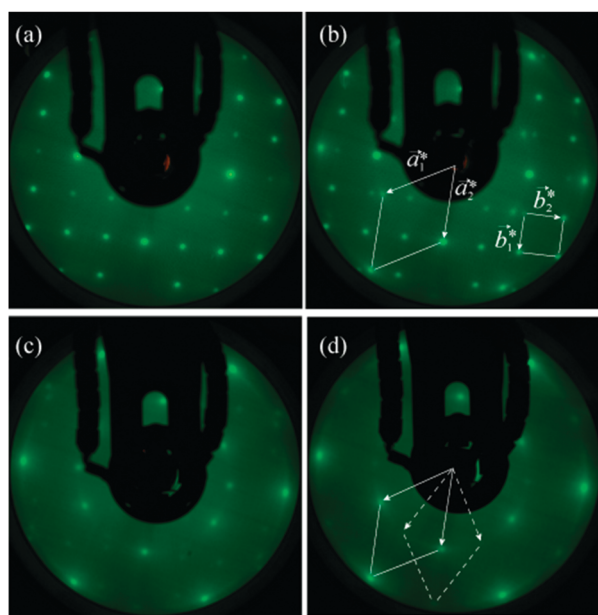


Fig. 2 LEED patterns (150 eV) obtained after (a) 2 min (b) 7 min, (c) 9 min (d) 12 min deposition of Mo on $\text{FeS}_2\{100\}$; the surface was flash annealed to 600 K after each deposition. Unit meshes and lattice vectors of the surface reciprocal lattices of $\text{MoS}_2\{0001\}$ and $\text{FeS}_2\{100\}$ (see text) are indicated in (b). Both primary and secondary (rotated by 30° from the latter) hexagonal patterns are indicated in (d).

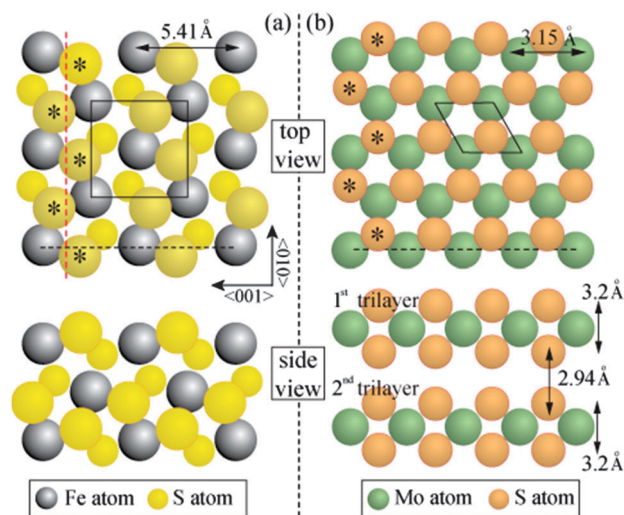


Fig. 3 Ball models for (a) $\text{FeS}_2\{100\}$ and (b) $\text{MoS}_2\{0001\}$ surface structures. The glide plane of the pyrite crystal is shown by the red broken line and is perpendicular to the page. The cross-sectional views along the grey broken lines are also plotted for each material. Asterisks mark the common S positions in the $\text{FeS}_2\{100\}$ and $\text{MoS}_2\{0001\}$ surface structures.

corresponding to a Mo/S AES peak height ratio of 0.11: the pattern is unchanged from that of the clean surface. An increase in the deposition time to a total of 7 min (Mo/S = 0.29), however, leads to the emergence of an additional hexagonal pattern, with a well-defined orientation relative to the coexisting square pattern of the substrate (Fig. 2b). At this relatively low Mo coverage the hexagonal pattern appears as low intensity, though quite sharp, spots whereas the square lattice spots remain sharp and intense. We ascribe the hexagonal pattern to the growth of regions of $\text{MoS}_2\{0001\}$. From the bulk lattice parameters of FeS_2 ($a = 5.416 \text{ \AA}$)¹³ and MoS_2 ($a = 3.16 \text{ \AA}$)¹⁴, as marked on the ball models of their structures in Fig. 3, it follows that the surface reciprocal lattice vectors have values $a_1^* = a_2^* = 2.30 \text{ \AA}^{-1}$ for $\text{MoS}_2\{0001\}$ and $b_1^* = b_2^* = 1.16 \text{ \AA}^{-1}$ for $\text{FeS}_2\{100\}$, i.e. a_1^* is within 1% of $2b_1^*$. Accordingly, certain spots of the hexagonal and square LEED patterns will coincide if the two lattices have the correct relative mutual orientation. The reciprocal vectors marked on the LEED pattern in Fig. 2b show that a_2^* is indeed coincident with $2b_1^*$. There is evidently a well-defined epitaxial relationship between the two real-space structures, which we discuss in detail below.

With further Mo deposition, the hexagonal pattern gradually intensifies whilst the square pattern fades away. Fig. 2c corresponds to a total 9 min deposition time and a Mo/S Auger peak height ratio of 0.35. At this coverage the square pattern corresponding to the $\text{FeS}_2\{100\}$ surface has almost completely disappeared. The spots of the hexagonal pattern show some slight streaking suggestive of a ring diffraction pattern. Moreover, a second hexagonal pattern, rotated 30° with respect to the initial one is also visible (most obviously in the outer ring of spots, indicated in Fig. 2d; more clearly visible after image processing, ESI† Fig. S1), albeit much less intense and more diffuse. The progressive disappearance of the original LEED pattern and intensification of the overlayer pattern are consistent with lateral growth of the $\text{MoS}_2\{0001\}$ regions until they cover the $\text{FeS}_2\{100\}$ substrate. In this case, our data suggest growth of $\text{MoS}_2\{0001\}$ domains with both primary and secondary orientations rotated by 30° from each other.



After a cumulative Mo deposition time of 12 minutes ($\text{Mo/S} = 0.46$) only the hexagonal pattern is visible (Fig. 2d). This exposure lies beyond the break of slope in the Fe/S ratio in Fig. 1, corresponding to a reduction of 92% in the Fe/S ratio relative to the pristine $\text{FeS}_2\{100\}$ surface. The complete suppression of the square lattice corresponding to $\text{FeS}_2\{100\}$, when probed at 150 eV electron kinetic energy, allows us to estimate the thickness of the MoS_2 layer at that particular coverage as being of the order of 1 nm, based on the fact that measured attenuation lengths of electrons in this energy range are normally 1 nm or less in solids.¹⁵ The Auger electrons used to assess compositional changes were of comparable energies and therefore probe approximately the same depth. We note that the clear break of slope of the Fe/S peak height ratio implies completion of growth of a layer of uniform thickness after 9 min deposition.

Further Mo deposition beyond 12 minutes progressively led to a higher diffuse background in the hexagonal LEED pattern, and eventually to the loss of any diffraction pattern. This was accompanied by a continuing linear increase in the Mo/S Auger peak height ratio. These observations indicate that a disordered Mo-rich layer forms on top of the ordered MoS_2 layer, rather than the overlayers stabilizing at an ordered stoichiometric $\text{MoS}_2(0001)$ structure. For exposures in excess of 12 minutes, longer anneals of up to 30 minutes were found to marginally sharpen the hexagonal LEED pattern, suggesting that S can diffuse through the Mo-rich overlayer, but with more difficulty than through the FeS_2 substrate. In light of the arguments below, there is no reason in principle why a thicker epitaxial $\text{MoS}_2(0001)$ film should not form on $\text{FeS}_2\{100\}$. The thickness of the ordered stoichiometric overlayer here is most likely S-diffusion-limited; we expect that co-deposition of S with Mo would be likely to lead to thicker epitaxial layers.

The formation of a thin film of MoS_2 on the FeS_2 substrate requires a driving force for S diffusion from one material to the other. Thermodynamically, MoS_2 (Gibbs free energy of formation $\Delta_f G^\circ = -225.9 \text{ kJ mol}^{-1}$) is more stable than FeS_2 ($\Delta_f G^\circ = -166.9 \text{ kJ mol}^{-1}$),¹⁶ which would drive S to react with deposited Mo and to form MoS_2 . A previous study by Kamaratos *et al.*¹⁷ of Fe adsorbed on $\text{MoS}_2\{0001\}$ found no evidence of Fe reacting with S from MoS_2 ; at high temperatures Fe simply desorbs. This is consistent with the higher thermodynamic stability of MoS_2 disfavoring diffusion of S from the MoS_2 substrate to sulphurize Fe. The inverse process, by contrast, seems to be facilitated, on the evidence of our experiments.

As noted above, the LEED data indicate that $\text{MoS}_2(0001)$ grows epitaxially on $\text{FeS}_2\{100\}$. This can be rationalised through the observation that the two materials share a common structural element. The structure of FeS_2 is based on that of rocksalt (NaCl), with the centroids of persulphide S_2^{2-} dimers located at anion sites, and the S-S dimer bonds oriented in $\langle 111 \rangle$ directions. This confers glide symmetry upon the $\{100\}$ surface, and leads to planes of S atoms lying above and below each plane of Fe atoms, to form an S-Fe-S trilayer structure (Fig. 3(a)). MoS_2 has a hexagonal crystal structure. S atoms are arranged hexagonally in both of two planes that lie above and below each plane of Mo atoms, to form an S-Mo-S trilayer structure (Fig. 3(b)); two trilayers are stacked within each bulk unit cell.

The relative orientation of the $\text{FeS}_2\{100\}$ and $\text{MoS}_2(0001)$ structures can be partially determined from the LEED patterns.

The glide symmetry of $\text{FeS}_2\{100\}$ causes a characteristic pattern of systematic absences of alternate beams along the direction parallel to the glide line.¹⁸ This feature constrains the possible orientation of the substrate: for the LEED pattern shown in Fig. 2a, the glide line runs from top to bottom. Individual S-Fe-S trilayers lack rotational symmetry, but successive trilayers are related by 180° mutual rotation. Fig. 3a depicts one of the two trilayers in an orientation that corresponds to the LEED pattern. It can be seen that the outer-lying S atoms in the top $\text{FeS}_2\{100\}$ trilayer are arranged in a zig-zag pattern. Fig. 3b depicts one trilayer of $\text{MoS}_2(0001)$; the orientation shown is consistent with that of the dominant hexagonal LEED pattern (Fig. 2b). The subset of S atoms marked * has an arrangement essentially identical to that of the zig-zag S rows of $\text{FeS}_2\{100\}$; the period matches to within 1%.

If we now overlay the $\text{MoS}_2(0001)$ trilayer over the $\text{FeS}_2\{100\}$ trilayer such that the common zig-zag rows coincide (Fig. 4), it emerges that the structure comes back almost exactly into coincidence after three repeats of the $\text{FeS}_2\{100\}$ unit mesh (five of the $\text{MoS}_2(0001)$) in the direction perpendicular to the common zig-zag S rows. A very slight elongation of the $\text{MoS}_2(0001)$ lattice in this direction ($< 3\%$) gives a perfect coincidence lattice structure. One possible scenario is that the common zig-zag row of S atoms is shared between the two structures, leading to S-Fe-S-Mo-S layering at the interface. Alternatively, both trilayers may be terminated by complete S layers, leading to S-Fe-S-S-Mo-S layering; in this scenario, the epitaxy is driven simply by van der Waals interactions between the layers. In principle, sourcing the S atoms in the MoS_2 layer from the bulk FeS_2 implies structural changes to the substrate. However, the quantity of S involved is negligible relative to the bulk concentration; moreover, we have previously shown that migration of bulk S to the surface facilitates self-healing of $\text{FeS}_2\{100\}$ after preferential S depletion during sputtering.¹² We conclude that the substrate structure is not significantly altered by growth of the MoS_2 film. Qualitative LEED observations cannot distinguish between the two suggested interface structures, but in either case it is the common zig-zag S rows that are the likely origin of the epitaxial growth that we observe. We emphasise that the well-defined epitaxial relationship

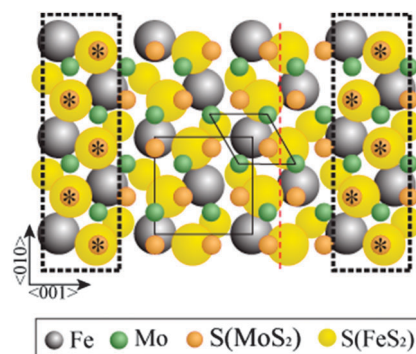


Fig. 4 Approximate lattice match obtained by laying $\text{MoS}_2(0001)$ surface structure on top of $\text{FeS}_2\{100\}$ at the orientations determined by the LEED patterns in Fig. 2. The matching S positions are highlighted within the dotted rectangles. The unit meshes for $\text{MoS}_2(0001)$ and $\text{FeS}_2\{100\}$ are noted as diamonds and squares, respectively. FeS_2 glide plane is shown by red dashed line.



between the two layers necessarily implies that the interface structure is crystallographically well defined.

Given that successive $\text{FeS}_2\{100\}$ trilayers are mutually rotated by 180° , the $\text{MoS}_2(0001)$ overlayer (which has 3-fold, not 6-fold, rotational symmetry) may be correspondingly rotated on successive substrate terraces, leading to two rotational domains of a single structure. Alternatively, rotating the overlayer through 180° relative to the substrate produces a structure which is formally distinct but which preserves the coincidence of the zig-zag S rows. The hexagonal LEED pattern shows 6-fold symmetry in all rings of spots at all energies, indicating the superposition of two 3-fold-symmetric patterns rotated by 180° (ESI,† Fig. S2). This is consistent with two rotational domains of a single structure, or equally with coexistence of the two distinct structures.

Rotating the $\text{MoS}_2(0001)$ trilayer through 30° would change the orientation of the hexagonal LEED pattern to that of the subsidiary hexagonal pattern seen in Fig. 2d. As shown in Fig. S3 of the ESI,† this also allows some measure of coincidence between S atoms in the $\text{MoS}_2(0001)$ and $\text{FeS}_2\{100\}$ structures. However, fewer S atoms are common to both structures, and the lattice matching is poorer, than in the dominant orientation. These factors are likely reasons for this orientation being the subsidiary one.

Finally, we comment on the thickness, morphology and uniformity of the $\text{MoS}_2(0001)$ film. The LEED and AES data are consistent with an overlayer thickness that is of the order of 1 nm and is uniform (based on the clear AES break of slope). From the bulk lattice parameter of MoS_2 , $c = 12.295 \text{ \AA}$,¹⁴ and the fact that each unit cell contains two S–Mo–S trilayers, we can deduce that the $\text{MoS}_2(0001)$ film is most likely two, and certainly between one and three, trilayers thick (see ESI,† for justification of this assertion). Individual $\text{MoS}_2(0001)$ domains are at least of the order of 100 \AA across. This is based on the fact that domains smaller than the LEED transfer width (usually taken to be of order 100 \AA)¹⁵ would lead to interference effects not seen in our data. Measurements made at different points on the sample verify that the $\text{MoS}_2(0001)$ film has uniform characteristics across the macroscopic area of the sample (of order 1 cm^2). The streaking seen in the LEED pattern implies slight rotational mosaicity of the $\text{MoS}_2(0001)$ layer. A similar effect is seen in LEED patterns obtained with graphene on $\text{Pt}\{111\}$ ¹⁹ and $\text{Cu}\{111\}$.²⁰ This may relate to local distortions or structural imperfections within individual $\text{MoS}_2(0001)$ domains (as observed for graphene by Gao *et al.*¹⁹ and Vázquez de Parga *et al.*²¹), or to different azimuthal orientations of individual domains (as suggested for graphene by Avila *et al.*²⁰).

In conclusion, few-layer films of highly ordered $\text{MoS}_2(0001)$ were formed on $\text{FeS}_2\{100\}$ by PVD of Mo and heating to 600 K to allow S to diffuse from the bulk substrate. The ordered $\text{MoS}_2(0001)$ overlayer was limited to a few layers' thickness, most probably two S–Mo–S trilayers. We attribute the facile epitaxial growth to the ready availability of S from the pyrite substrate; a strong thermodynamic driving force for the formation of MoS_2 in preference to FeS_2/FeS ; and the well-defined lattice relationship and common

structural element between the $\text{MoS}_2(0001)$ and $\text{FeS}_2\{100\}$ surfaces. Grown this way, the MoS_2 layer is already in intimate, crystallographically well-defined contact with the semiconducting substrate. This approach paves a promising possible way forward for the development of practical devices with 2D MoS_2 .

The authors thank the EPSRC (grant ref. EP/E039782/1) for funding.

Notes and references

- 1 L. Rodríguez-Pérez, M. A. Herranz and N. Martín, *Chem. Commun.*, 2013, **49**, 3721.
- 2 (a) R. Mas-Ballesté, C. Gómez-Navarro, J. Gómez-Herrero and F. Zamora, *Nanoscale*, 2011, **3**, 20; (b) Q. H. Wang, K. Kalantar-Zadeh, A. Kis, J. N. Coleman and M. S. Strano, *Nat. Nanotechnol.*, 2012, **7**, 699; (c) M. Xu, T. Liang, M. Shi and H. Chen, *Chem. Rev.*, 2013, **113**, 3766.
- 3 (a) W. O. Winer, *Wear*, 1967, **10**, 422; (b) M. Vrinat, M. Breyssse, C. Geantet, J. Ramirez and F. Massoth, *Catal. Lett.*, 1994, **26**, 25.
- 4 B. Radisavljevic, A. Radenovic, J. Brivio, V. Giacometti and A. Kis, *Nat. Nanotechnol.*, 2011, **6**, 147.
- 5 (a) K. F. Mak, C. Lee, J. Hone, J. Shan and T. F. Heinz, *Phys. Rev. Lett.*, 2010, **105**, 136805; (b) A. Splendiani, L. Sun, Y. Zhang, T. Li, J. Kim, C.-Y. Chim, G. Galli and F. Wang, *Nano Lett.*, 2010, **10**, 1271.
- 6 (a) D. Xiao, G. B. Liu, W. Feng, X. Xu and W. Yao, *Phys. Rev. Lett.*, 2012, **108**, 196802; (b) H. Zeng, J. Dai, W. Yao, D. Xiao and X. Cui, *Nat. Nanotechnol.*, 2012, **7**, 490; (c) K. F. Mak, K. He, J. Shan and T. F. Heinz, *Nat. Nanotechnol.*, 2012, **7**, 494.
- 7 W. Wu, L. Wang, Y. Li, F. Zhang, L. Lin, S. Niu, D. Chenet, X. Zhang, Y. Hao, T. F. Heinz, J. Hone and Z. L. Wang, *Nature*, 2014, **514**, 470.
- 8 O. Frank and M. Kalbac, Chemical vapour deposition (CVD) growth of graphene films, in *Graphene: Properties, Preparation, Characterisation and Devices*, ed. V. Skákalová and A. B. Kaiser, Woodhead Publishing, 2014.
- 9 (a) Y. Zhan, Z. Liu, S. Najmaei, P. M. Ajayan and J. Lou, *Small*, 2012, **8**, 966; (b) Y.-H. Lee, X.-Q. Zhang, W. Zhang, M.-T. Chang, C.-T. Lin, K.-D. Chang, Y.-C. Lu, J. T.-W. Wang, C.-S. Chang, L.-J. Li and T.-W. Lin, *Adv. Mater.*, 2012, **24**, 2320; (c) K.-K. Liu, W. Zhang, Y.-H. Lee, Y.-C. Lin, M.-T. Chang, C.-Y. Su, C.-S. Chang, H. Li, Y. Shi, H. Zhang, C.-S. Lai and L.-J. Li, *Nano Lett.*, 2012, **12**, 1538; (d) Y. Shi, W. Zhou, A.-Y. Lu, W. Fang, Y.-H. Lee, A. L. Hsu, S. M. Kim, K. K. Kim, H. Y. Yang, L.-J. Li, J.-C. Idrobo and J. Kong, *Nano Lett.*, 2012, **12**, 2784.
- 10 (a) S. Helveg, J. V. Lauritsen, E. Lægsgaard, I. Stensgaard, J. K. Nørskov, B. S. Clausen, H. Topsøe and F. Besenbacher, *Phys. Rev. Lett.*, 2000, **84**, 951; (b) J. Kibsgaard, J. V. Lauritsen, E. Lægsgaard, B. S. Clausen, H. Topsøe and F. Besenbacher, *J. Am. Chem. Soc.*, 2006, **128**, 13950.
- 11 A. K. Geim and I. V. Grigorieva, *Nature*, 2013, **499**, 419.
- 12 (a) T. Liu, I. Temprano, S. J. Jenkins, D. A. King and S. M. Driver, *Phys. Chem. Chem. Phys.*, 2012, **14**, 11491; (b) T. Liu, I. Temprano, S. J. Jenkins, D. A. King and S. M. Driver, *J. Phys. Chem. C*, 2013, **117**, 10990.
- 13 E. D. Stevens, M. L. DeLucia and P. Coppens, *Inorg. Chem.*, 1980, **19**, 813.
- 14 H. E. Swanson, N. T. Gilfrich and G. M. Ugrinic, *NBS Circular 539*, 1955, vol. 5.
- 15 D. P. Woodruff and T. A. Delchar, *Modern Techniques of Surface Science*, Cambridge University Press, 2nd edn, 1994.
- 16 *CRC Handbook of Chemistry and Physics*, ed. W. M. Haynes, Taylor and Francis, 95th edn, 2014.
- 17 M. Kamaratos and C. A. Papageorgopoulos, *Surf. Sci.*, 1985, **160**, 451.
- 18 B. Holland and D. P. Woodruff, *Surf. Sci.*, 1973, **36**, 488.
- 19 M. Gao, Y. Pan, L. Huang, H. Hu, L. Z. Zhang, H. M. Guo, S. X. Du and H.-J. Gao, *Appl. Phys. Lett.*, 2011, **98**, 033101.
- 20 J. Avila, I. Rizado, S. Lorc, R. Fleuri, E. Pichonat, D. Vignaud, X. Wallart and M. C. Asensio, *Sci. Rep.*, 2013, **3**, 8.
- 21 A. L. Vázquez de Parga, F. Calleja, B. Borca, M. C. G. Passeggi, J. J. Hinarejos, F. Guinea and R. Miranda, *Phys. Rev. Lett.*, 2008, **100**, 056807.

